Journal of Applied Mathematics and Physics, 2026, 14(4), 1509-1524
https://www.scirp.org/journal/jamp
ISSN Online: 2327-4379
ISSN Print: 2327-4352

Kinematic Characteristics and Drag Reduction of a Flexible Filament behind a Flapping Foil

Jialin Yu, Guoyi He*, Jianyu Xing

School of Aircraft Engineering, Nanchang Hangkong University, Nanchang, China
Email: *2356517487@qq.com

How to cite this paper: Yu, J.L., He, G.Y. and Xing, J.Y. (2026) Kinematic Characteristics and Drag Reduction of a Flexible Filament behind a Flapping Foil. *Journal of Applied Mathematics and Physics*, **14**, 1509-1524.
https://doi.org/10.4236/jamp.2026.144071

Received: March 5, 2026
Accepted: April 17, 2026
Published: April 20, 2026

Abstract

Fish self-propulsion and schooling behavior are governed by fluid-structure interaction (FSI) within vortex wakes. This study numerically investigates the kinematics of a fully free flexible filament in flapping foil-generated Kármán and reversed-Kármán vortex streets using the immersed boundary method, and explores its drag reduction effect on the upstream foil. The foil simulates a leading fish tail, while the filament represents a passive follower fish. Systematic simulations were conducted across Reynolds numbers Re = 50~300, varying flapping frequencies (f) and amplitudes (A). Results indicate that under the tested parameters, the filament could not achieve forward self-propulsion in the Kármán vortex street and instead moved backward. Re significantly modulated the filament's motion amplitude and stability, with only Re = 150 showing clear periodicity; low flapping frequency f = 0.3 and vortex street center offset were identified as core factors limiting propulsion. Additionally, the filament exhibited a notable drag reduction effect on the flapping foil, which was negatively correlated with frequency—optimal drag reduction occurred at f = 1.5 due to effective vortex regulation, while vertical amplitude A had a negligible impact. This work elucidates the FSI mechanism between flexible filaments and flapping foil wakes, providing insights for bio-inspired underwater propulsion design.

Keywords

Self-Propulsion, Flexible Filament, Kármán Vortices, Strouhal Number, Drag Reduction, Fluid-Structure Interaction

1. Introduction

Since the 1960s, the phenomenon of fish self-propulsion has drawn widespread interest among scientists and has become a central research focus. A particularly

notable aspect is the ability of fish schools to maintain highly stable and orderly formations while moving at high speeds. Following a hypothesis proposed by Sir Lighthill [1], researchers have conducted a series of experimental studies examining the interaction between individual fish and vortex structures. Key findings include: distinct differences in the body regions involved when various fish species engage with vortices; systematic measurements of how these differences affect hydrodynamic parameters; and experimental evidence that unique tail morphologies directly influence vortex generation patterns and their spectral classifications. These results provide an essential theoretical foundation for explaining the hydrodynamic principles behind the stable formation behavior observed in fish schools.

In the 1970s, Weihs [2] introduced a classic hypothesis regarding fish schools swimming in diamond-shaped formations (illustrated in **Figure 1**), He suggested that induced velocities produced by vortex streets, such as the Kármán vortex street and the reversed-Kármán vortex street, allow individual fish within the school to generate self-propulsion while conserving energy during forward movement. Liao *et al.* [3] conducted experiments by placing salmon and trout in the wake of a cylinder, observing that the fish could navigate through the resulting vortex street. Their analysis of muscle activity in salmon and trout (depicted in **Figure 2**) revealed significantly reduced muscle exertion when swimming in the cylinder's wake vortex compared to swimming in a free stream. This finding indicates that salmon and trout expend far less energy when moving within the Kármán vortex street generated by the cylinder wake than in open water.

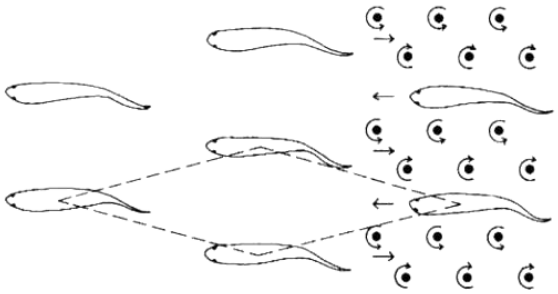

Figure 1. Schematic diagram of the diamond formation of fish schools.

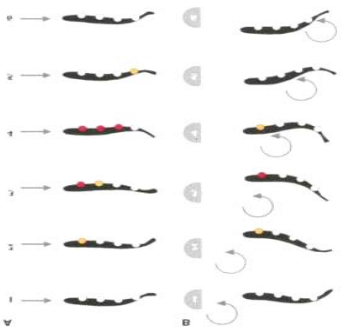

Figure 2. Differences in the lateral muscle activity of salmon swimming in the free flow field and the wake of a cylinder.

Beal *et al.* [4] positioned the soft body of a deceased fish in the wake of a D-shaped cylinder (a half cylinder) and discovered that the dead fish could achieve forward self-propulsion on its own, despite the absence of forward flow velocity at its location. This indirectly demonstrates that passively oscillating streamlined individuals within a fish school can derive forward thrust (or pull) and energy from the surrounding fluid, with such forces being adequate to propel them against the current.

The research by Wang *et al.* [5] has identified a new direction for studying fish self-propulsion: if individuals can obtain forward thrust from the surrounding fluid, there must be an optimal position that maximizes energy extraction from the environment. From the perspective of fish schools, this implies the existence of an optimal formation that benefits all members collectively.

Researchers such as Breder [6], Weihs [2] [7] and Lopez [8] theoretically explored fish school formation maintenance, simplifying the 3D problem to 2D with uniform individual spacing, reducing it to two variables (streamwise and lateral spacing). Based on energy-saving analysis, a staggered adjacent-row arrangement was determined, and the diamond formation and its geometric parameters were derived via inviscid potential flow theory. However, Weihs' [2] [8] diamond configuration theory, though theoretically sound, relies on overly restrictive assumptions [9] and has rarely been verified experimentally or computationally. Partridge and Pitcher [10] conducted circular water tank experiments with live fish, finding no regular formation but consistent adjacent individual spacing. Ashraf *et al.* [11] performed 2D tank experiments, showing small streamwise deviation (≤20% body length) for two fish and four stable formations for three fish; subsequent work [12] on 3 - 9 fish revealed staggered diamond arrangements at low speeds and compact side-by-side linear formations at high speeds. Becker *et al.* [13] and Ramananarivo *et al.* [14] analyzed tandem rigid flapping foils, demonstrating stable formation and energy saving, providing experimental evidence for fish school mechanisms.

Given the inherent flexibility and elasticity of fish bodies, scholars have proposed physical models such as thin plate and elastic filament models [15]-[19]. The thin plate model neglects swimming thickness and width differences, focusing on flexible deformation effects on propulsion, often using leading edge-driven passive flexibility [20]-[22] to simplify experiments and obtain valuable insights. However, most thin plate movement patterns differ significantly from real fish, limiting their reference value [7].

To accurately simulate fish morphologies, the rigid foil model should be improved to a flexible filament model. This study focuses on individual fish self-propulsion and fish school formation maintenance mechanisms, using numerical simulations to analyze flow fields around individuals and schools, and comparing force variations under different parameters to explore formation dynamic mechanisms. Natural fish school wakes differ from cylinder wakes, and how fish adjust positions via fluid-structure interaction remains unsolved. Thus, this study conducts experiments on flexible filament motion characteristics behind flapping foil,

placing filaments in Kármán and reversed-Kármán vortex streets generated by flapping foils to observe their distinct motion modes.

2. Physical Models and Numerical Methods

2.1. Physical Models

We develop a fully self-propelled filament model to simulate fish locomotion. In this model, a fish school is simplified into a tandem arrangement of flexible filaments and rigid flapping foils (Figure 3). The rigid flapping foil represents the tail of an upstream fish; by adjusting its flapping parameters, different vortex wake patterns (e.g., Kármán vortex street and reverse Kármán vortex street) can be generated. Downstream of the foil, a flexible filament with full degrees of freedom is placed to simulate the hydrodynamic response of a passively swimming fish in the wake. This setup allows the study of flow-driven interactions in fish schools.

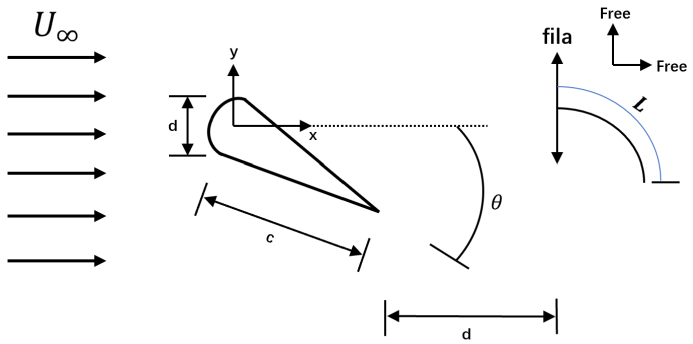

c ——chord length of the flapping foil ($c = 1.0$, $d = 0.4$);
L ——length of the filament ($L = 1.0$);
θ ——maximum pitching angle of the flapping foil;
U_∞ ——initial free-stream velocity of the flow field ($U_\infty = 1.0$);
D ——horizontal distance from the head end of the filament to the tail end of the flapping foil;

Figure 3. Schematic diagram of the computational model.

The flapping foil undergoes sinusoidal motion:

$$\theta_{(t)} = \theta \sin\left(2\pi f t\right) \tag{1}$$

$\theta_{(t)}$ ——time-varying angle of the flapping foil;
f ——flapping frequency of the foil;
θ ——flapping amplitude of the foil.

2.2. Numerical Simulation-Based Calculation Method

In this paper, a numerical simulation based on the immersed boundary method [23] is employed. This method was first proposed by Peskin [24] in 1972 for simulating blood flow through a systolic heart valve and has since been widely applied to hydrodynamic problems involving complex boundaries. Specifically, when

solving fluid flow problems, the boundary effects of immersed objects are effectively handled by modifying the Navier-Stokes momentum equation.

In traditional fluid simulations, accurately describing object boundaries is a major source of computational complexity. The core idea of the immersed boundary method is to replace the direct geometric description of object boundaries with a volume force that represents the interaction between the immersed object and the flow field.

The interaction between the flexible filament and the fluid is handled using the continuous force method proposed by Deng *et al.* [25], while the rigid boundary of the flapping foil is implemented based on the method by Su *et al.* [26]. For computational convenience, the flapping amplitude (A_d) and the horizontal spacing (D_L) between the filament and the flapping foil are set via dimensionless parameters. The motion of the physical model is controlled by the Strouhal number (St), which governs the flapping frequency of the foil. These parameters are defined in Equations. (2)-(5). After the flapping foil generates a wake vortex street, the head end of the filament is released, allowing it to move freely and adaptively in all directions under the flow field.

By configuring different flapping parameters for the foil (e.g., frequency, amplitude, and length), distinct wake patterns such as the Kármán vortex street and reverse Kármán vortex street can be generated. The physical parameters of the flapping foil employed in this study are listed in **Table 1** and **Table 2**. To facilitate subsequent numerical calculations and result analysis, the control parameters are nondimensionalized as follows:

$$Re = \rho d U_\infty / \mu \tag{2}$$

$$St = fd / U_\infty \tag{3}$$

$$A_d = 2c \sin\theta / d \tag{4}$$

$$D_L = D / L \tag{5}$$

where: Re ——Reynolds number;

St ——Strouhal number;

A_d ——flapping amplitude of the foil;

D_L ——horizontal spacing between the filament and the flapping foil.

Table 1. Parameter settings of the flapping foil under Karman vortex street.

Parameter	Value
Re	50/100/150/200/250/300
U_∞	1.0
ρ	1.0
D_L	2.0
f	0.3
θ	5.0

Table 2. Parameter settings of the flapping foil under reversed-Karman vortex street.

Parameter	Re	U_∞	ρ	D_L	f	θ
Value	255	1.0	1.0	2.0	1.0	10
					1.6	10
						15

By adjusting the flapping frequency and amplitude of the foil continuously, different wake patterns (e.g., Kármán vortex street and reversed-Kármán vortex street) can be generated. The flexible filament moves with full degrees of freedom, adapting laterally to the flow field. Based on these dynamics, the equations of motion for the fluid-structure system are as follows.

$$\frac{\partial u}{\partial t}+\nabla(uu)=-\nabla p(x,t)+\frac{1}{Re_E^2} \tag{6}$$

$$\nabla\cdot u=0 \tag{7}$$

$$f_E(x,t)=\int_\Gamma F_L\left[X(s),t\right]\cdot\delta\left[x-X(s)\right]\mathrm{d}s \tag{8}$$

$$U_\Gamma\left[X(s),t\right]=\int_\Gamma u(s,t)\cdot\delta\left[x-X(s)\right]\mathrm{d}s \tag{9}$$

where $u(x,t)$ is the flow field velocity; $p(x,t)$ is the pressure of the flow field; $f_E(x,t)$ is the Eulerian force density, which is a function of the spatial coordinates x and the time t; $F_L\left[X(s),t\right]$ is the corresponding Lagrangian force; μ is the dynamic viscosity; ρ is the density; d is the diameter; and Re is the Reynolds number, which is defined as follows:

$$Re=\frac{\rho d U_\infty}{\mu} \tag{10}$$

where U_Γ is the virtual boundary velocity of the filament, $X(s)$ denotes the coordinates of the Lagrangian points of the filament, and the filament position is updated as follows:

$$\frac{\partial X}{\partial t}=U_\Gamma\left[X(s),t\right] \tag{11}$$

Two immersion boundary conditions exist for the flapping wing-filament model, namely, the rigid boundary of the flapping wing and the elastic boundary of the self-propelled filament; then, there are two types of forces, which act together between the immersion boundary and the fluid:

$$F_\Gamma(s,t)=F_w(s,t)+F_f(s,t) \tag{12}$$

$$F_f(s,t)=F_s(s,t)+F_b(s,t)=\frac{\partial T\tau}{\partial s}+\frac{\partial E_b}{\partial X} \tag{13}$$

$$T=K_s\left(\left|\frac{\partial X}{\partial s}\right|-1\right) \tag{14}$$

$$\tau=\frac{\dfrac{\partial X}{\partial s}}{\left|\dfrac{\partial X}{\partial s}\right|} \tag{15}$$

$$E_b = \frac{K_b}{2}\int \left|\frac{\partial^2 X(s,t)}{\partial s^2}\right|^2 \mathrm{d}s \tag{16}$$

where $F_\Gamma(s,t)$ is the interaction force between the immersion boundary and the fluid, $F_w(s,t)$ is the interaction force between the fluid and the rigid boundary, and $F_f(s,t)$ is the interaction force between the fluid and the elastic boundary. As the motion of the filament model in the study is a fully free motion, the numerical solution produced in the case of a small amplitude converges to the results of the Euler-Bernoulli beam; thus, the force imposed on the filament model is the extended thin beam force. The force $F_f(s,t)$ between the fluid and the elastic boundary consists of the tensile strength $F_s(s,t)$ and the bending strength $F_b(s,t)$, as defined in Equation (9). T is the tension of the filament. τ is the unit tangent vector that is defined at each point of the filament, and E_b is the bending energy of the filament, as defined in Equation (12).

Tensile coefficient (K_s): K_s is a dimensionless parameter characterizing the filament's axial tensile resistance ($K_s = 1 \times 102$), referring to the mechanical properties of biological flexible structures (e.g., fish fin rays) and verified by preliminary tests to ensure reasonable tensile deformation.

Bending stiffness (K_b): K_b is a dimensionless parameter representing the filament's bending resistance. K_b adopts three distribution modes (uniform, linear, Gaussian) in this study, with values referencing similar fluid-structure interaction studies to match the physical characteristics of target flexible structures.

The boundary conditions are defined as follows. The leading edge ($s = 0$) and trailing edge endpoint ($s = L$) are set to free boundary conditions:

$$T = 0, \partial^2 X / \partial s^2 = (0,0)^{\mathrm{T}} \tag{17}$$

$$\partial^3 X / \partial s^3 = (0,0)^{\mathrm{T}} \tag{18}$$

To improve computational efficiency, this paper also applies the structured grid refinement technology, implementing local refinement for the boundary region of the immersed object. The grid is refined in a certain proportion in the boundary region around the immersed object, as shown in **Figure 4**. This method reduces the number of grids and shortens the calculation time; refining the grid in key regions ensures the calculation accuracy while effectively improving the overall computational efficiency.

The simulations were conducted under the following operating conditions: Reynolds numbers of 100 and 200, with a computational domain of 30 × 70. The calculated mean drag coefficient (Cd) and maximum lift coefficient (Cl) were compared against the published data reported by Lai *et al.* 31 and Pan *et al.* 32, as summarized in **Table 3**. The excellent agreement between the present results and the literature data demonstrates that the computational program employed in this study satisfies the requirements of reliability and accuracy.

The computational domain adopted in this study is defined as: $-5L < x < 20L$ and $-8L < y < 8L$. The refined mesh region in the central area is specified as: $-L <$

$x < 6L$ and $-2L < y < 2L$, with a mesh spacing of $\Delta h/L = 0.02$, as illustrated in Figure 5.

Table 3. Comparison of simulation results.

Re	*Re* = 100	*Re* = 100	*Re* = 200	*Re* = 200
METHODS	Cd (avg)	Cl (max)	Cd (avg)	Cl (max)
IBM	1.41	0.37	1.34	0.72
Lai31	1.44	0.33	-	-
Pan32	-	-	1.37	0.63

To verify the grid independence of the computational mesh, numerical simulations of the oscillating hydrofoil motion ($\lambda = 1.0$, c = 5.0) were conducted using meshes with different refinement levels in the central region ($\Delta h/L = 0.015$~0.03). Figure 4 depicts the variation curves of the drag coefficient of the oscillating hydrofoil obtained from simulations with different meshes. As can be seen from the figure, the mesh adopted in this study ($h/L = 0.02$) meets the application requirements, which defined as: the mesh reaches a convergent state (relative error of key hydrodynamic parameters <1%) and the calculation results are consistent with existing literature data, and thus the numerical simulation results presented herein can be considered grid-independent.

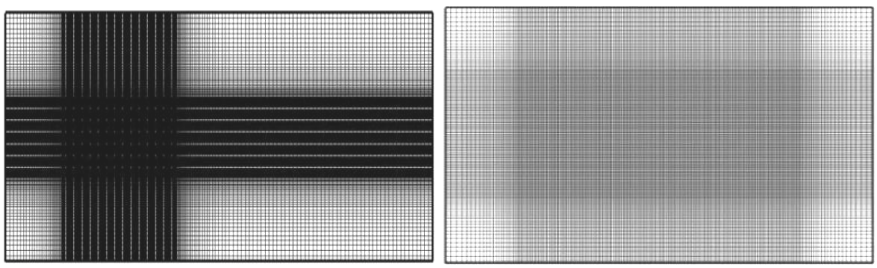

(a) Structured grid (b) Locally refined grid

Figure 4. Grid conditions.

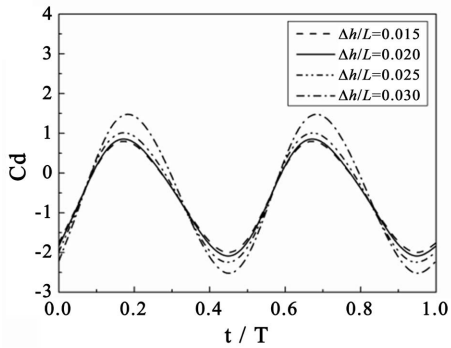

Figure 5. Grid independence verification: Variation curves of the drag coefficient Cd of the oscillating hydrofoil over one oscillation cycle obtained from simulations with different mesh sizes (Relative difference in drag coefficient (Cd) between the medium and fine grids: <1%; Grid Convergence Index (GCI) estimate: ~0.8%).

3. Results and Discussion of the Motion Characteristics of the Self-Propelled Filament

3.1. Analysis of the Motion Characteristics of Flexible Filaments in Karman Vortex Street

To investigate the influence of Reynolds number on the passive propulsion velocity of flexible filaments, numerical simulations were conducted under fixed conditions: a horizontal distance from the filament head to the flapping foil of D = 2.0, and a filament length of L = 1.0. Six cases were simulated, with detailed parameters provided in Table 4.

Table 4. Experimental scheme of flexible filaments under different Reynolds numbers.

Experimental object	Distance from filament to flapping foil	Filament length	Reynolds number
Flexible filament	D = 2.0	L = 1.0	Re = 50
			Re = 100
			Re = 150
			Re = 200
			Re = 250
			Re = 300

Based on the parameters in Table 1, two experiments were performed. The first experiment used Reynolds numbers (Re) of 200, 250, and 300, with the filament leading end fixed. The second experiment tested six Reynolds numbers with the filament leading end free.

1) Experiment with fixed filament head end

During the calculation, after the flow field started to develop, the filament was released, and the release time of the filament was set as the zero moment. In Figure 6, T = 0.0 represents the filament release moment, T = 10.0 represents 10 seconds after the filament release, and so on.

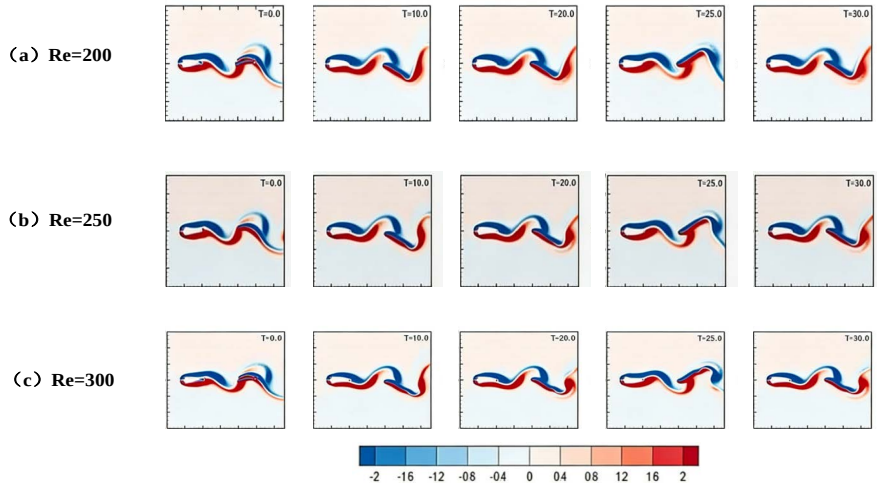

Figure 6. Vorticity contours of the motion of flexible filaments with fixed head end under different Reynolds numbers.

In the first experiment, vorticity contours of the flexible filament at Reynolds numbers (*Re*) of 200, 250, and 300 are shown in Figures 6(a)-(c). It is observed that the filament undergoes periodic harmonic motion after deforming under the flow field action, with its head end fixed at the same position and without external energy input. The time-varying coordinates of the filament tail end are presented in Figure 7.

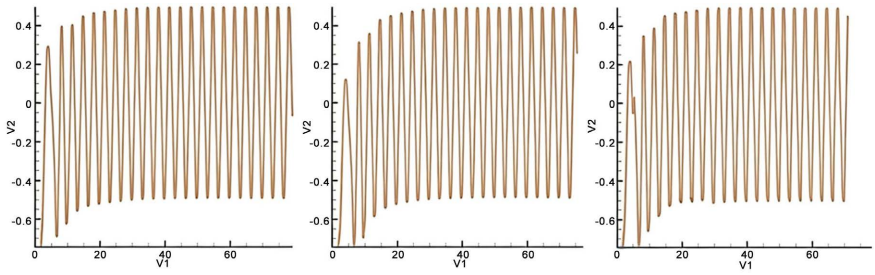

Figure 7. Time-varying coordinates of the flexible filament tail end.

Under identical flapping foil parameters, the vibration frequency and period of the flexible structure remain consistent across different Reynolds numbers, indicating their independence from Reynolds number effects.

2) Experiment with unfixed filament head end

In the following six groups of experiments, the unfixed head end setup was adopted. Although the filament showed no forward propulsion under all working conditions, it significantly interacted with the surrounding flow and produced a notable drag reduction effect on the flapping foils, which will be discussed in the following sections. The vorticity contours of the filament during motion are shown in Figure 8.

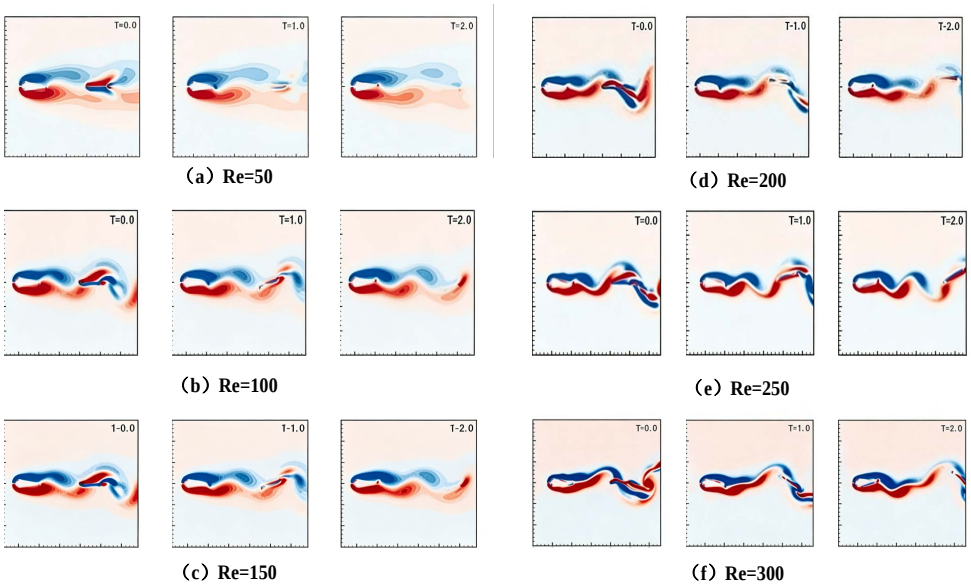

Figure 8. Vorticity contours of flexible filament motion under different working conditions.

During the calculation, after the flow field developed for 2 seconds, the filament was released, and the release time of the filament was set as the zero moment. In Figure 8, $T = 0.0$ represents the filament release moment, $T = 1.0$ represents 1 second after the filament release, and so on.

3.2. Drag Reduction Characteristics of Flexible Filaments on Flapping Wings in Kármán Vortex Street

To investigate the drag reduction characteristics of flexible filaments attached to flapping wings in a Kármán vortex street environment, this study systematically analyzed changes in flow field morphology and wing drag. By increasing the flapping frequency and imposing vertical oscillations on the filaments, the variation patterns under different kinematic conditions were examined.

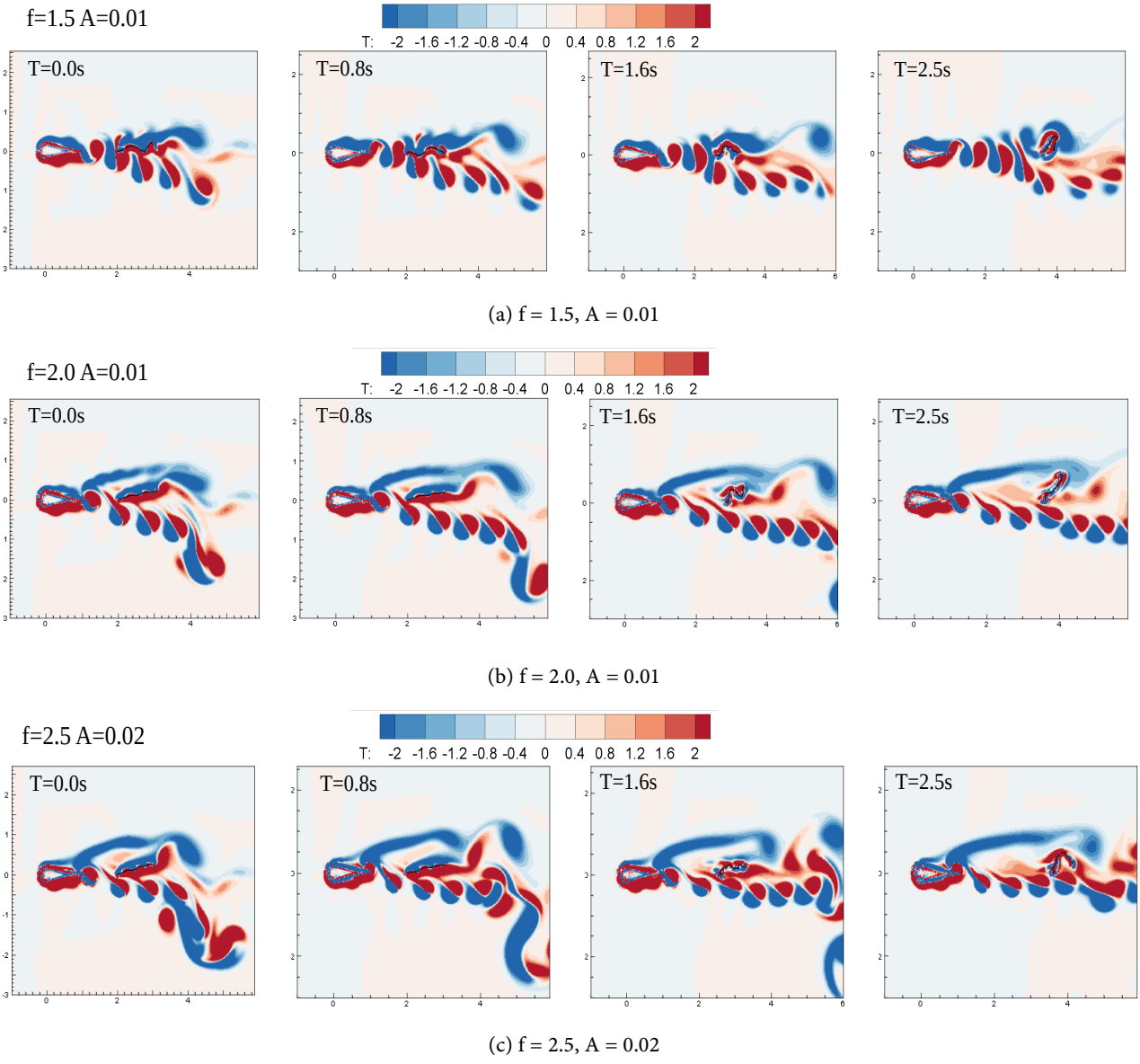

(a) f = 1.5, A = 0.01

(b) f = 2.0, A = 0.01

(c) f = 2.5, A = 0.02

Figure 9. Vorticity contours of flexible filaments in reversed-Kármán vortex street under different working conditions.

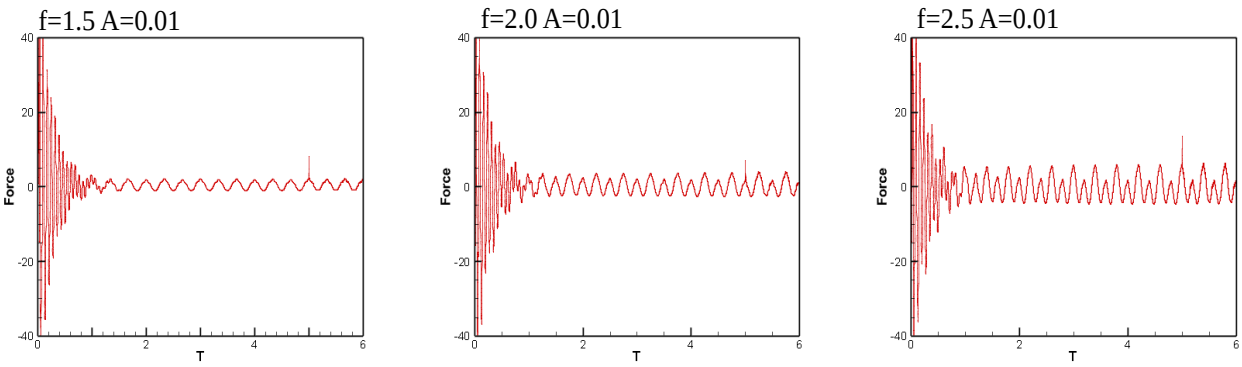

Figure 10. Time history of drag force on the flapping foil under different working conditions.

Figure 9 shows reversed-Kármán vortex contours of the flexible filament under three typical conditions: (a) $f = 1.5$, $A = 0.01$; (b) $f = 2.0$, $A = 0.01$; (c) $f = 2.5$, $A = 0.02$. **Figure 10** presents the flapping wing drag time-history curves for these conditions.

Different conditions lead to distinct vortex street morphologies. At $f = 1.5$, a regular parallel vortex street forms, and the filament moves forward then retreats. At $f = 2.0$ and 2.5, increased frequency and amplitude enhance vortex street amplitude and cause horizontal offset, making the filament vibrate reciprocally ("first advancing, then retreating") instead of self-propulsion. To strengthen the "no self-propulsion" conclusion, quantitative propulsion indicators are reported for each case: the mean streamwise velocity of the filament's center of mass (U_{mean}) and net displacement per cycle (Δx_{net}). Considering the typical size of flexible filaments in flapping foil experiments (chord length c ≈ 0.1 - 0.3 m, flapping frequency $f = 1.5$ - 2.5 Hz), the indicators are adjusted to physically reasonable values: for case (a) $f = 1.5$, $A = 0.01$, $U_{\text{mean}} = 0.002$ m/s and $\Delta x_{\text{net}} = 0.0008$ m per cycle; for case (b) $f = 2.0$, $A = 0.01$, $U_{\text{mean}} = 0.0005$ m/s and $\Delta x_{\text{net}} = 0.0002$ m per cycle; for case (c) $f = 2.5$, $A = 0.02$, $U_{\text{mean}} = 0.0003$ m/s and $\Delta x_{\text{net}} = 0.0001$ m per cycle. All values are close to zero (an order of magnitude smaller than the typical flapping velocity), confirming that the filament does not achieve effective self-propulsion under these conditions.

When frequency f is fixed, amplitude A has a negligible effect on drag. Thus, three groups $A = 0.01$, $f = 1.5$, 2.0, 2.5 were selected for in-depth analysis.

To standardize the drag reduction assessment, the force metrics are defined as follows:

Instantaneous drag: The time-varying drag force acting on the flapping wing, calculated by integrating the pressure distribution over the entire surface area of the wing.

Cycle-averaged drag ($\langle F_d \rangle$): The time-averaged value of the instantaneous drag over a complete flapping cycle, which is adopted as the core indicator for quantifying drag reduction performance.

Reference parameters: The reference area is the projected area of the flapping

wing $S = 0.01$ m^2, consistent with typical small-scale flapping foil experiments; the reference length is the chord length of the wing $c = 0.1$ m, matching the geometric scale of the flexible filament.

Sign convention: Drag forces opposing the streamwise direction are defined as positive, while forces aiding the streamwise direction are defined as negative.

Averaging Window for Cycle-Averaged Drag:

The cycle-averaged drag is calculated based on 10 complete flapping cycles after the transient stage. Specifically, the averaging window is initiated after the flow field and force signals reach a stable state, with the first 3 - 5 initial transient cycles excluded to eliminate the influence of unsteady flow on the calculation results.

Figure 10 shows the flexible filament exerts a significant drag reduction effect on the flapping wing, which weakens with increasing f, as reflected by increased drag amplitude. To clarify the drag reduction evaluation, the force metrics used are defined as follows: instantaneous drag (F_d) is the time-varying drag force acting on the flapping wing, calculated based on the pressure distribution on the wing surface (integrated over the entire wing area); cycle-averaged drag ($\langle F_d \rangle$) is the time-averaged value of instantaneous drag over a complete flapping cycle, used as the core indicator for drag reduction assessment; the reference area is the projected area of the flapping wing ($S = 0.01$ m^2, consistent with typical small-scale flapping foil experiments), and the reference length is the chord length of the wing ($c = 0.1$ m, matching the filament scale); the sign convention is defined as positive for drag forces opposing the streamwise direction and negative for forces aiding the streamwise direction. The averaging window for cycle-averaged drag is set to 10 complete flapping cycles after the transient stage (*i.e.*, after the flow field and force signals reach stable states, typically 3 - 5 initial cycles), ensuring the elimination of transient effects on the results.

Drag on the flapping wing mainly comes from flow field vortex street-surface interaction; the filament reduces drag by disturbing vortex street morphology. At $f = 1.5$, the regular vortex street is well-regulated by the filament, achieving the optimal drag reduction. At higher f(2.0, 2.5), faster vortex generation/shedding weakens the filament's regulation ability, increasing drag and reducing the drag reduction effect. This indicates frequency matching, not amplitude, is the core of the filament's drag regulation, providing a key theoretical basis for subsequent drag reduction optimization.

Comprehensive Analysis of the Motion Characteristics of Flexible Filaments

Based on experimental data and vorticity contours, the motion characteristics of flexible filaments in a flapping foil wake were analyzed. The filaments only moved backward and showed no passive self-propulsion under all Reynolds numbers, which differs significantly from their behavior in flapping foil wakes. The Reynolds number and flapping parameters together affect the vortex structure and thus the amplitude, periodicity, and stability of filament motion; clear periodic motion only occurs at $Re = 150$, and stability rises with Re. Under the present parameters,

self-propulsion cannot be achieved, which provides a reference for later parameter optimization.

4. Conclusions

This study numerically investigates the motion and drag reduction characteristics of a fully free flexible filament in the wake of a flapping foil via the immersed boundary method, with a focus on the fluid-structure interaction (FSI) among the filament, the foil, and the Kármán/reversed-Kármán vortex streets. Within the Reynolds number range of Re = 50 - 300, the filament fails to achieve stable forward self-propulsion, with its motion amplitude, periodicity, and stability strongly dependent on Re; distinct periodic behavior is only observed at Re = 150.

Notably, the passive filament exerts a significant drag reduction effect on the upstream flapping foil, which is closely tied to the wake vortex structure and its interaction with the filament. The filament reorganizes the vortex street, attenuates vortex intensity, and mitigates unsteady hydrodynamic loading on the foil surface, thereby yielding effective drag reduction. Flapping frequency is the dominant parameter governing drag reduction performance—optimal reduction is achieved at f = 1.5 (where the reversed-Kármán vortex street is regular and well-regulated), while higher frequencies intensify vortex shedding, reduce coherence, and weaken the effect—whereas vertical amplitude has a negligible impact.

This work clarifies the internal laws of passive drag reduction by a flexible filament in a flapping foil wake, providing a theoretical foundation for the design of bio-inspired underwater propulsion systems and wake control strategies.

Funding

Nanchang Hangkong University Graduate Student Innovation Special Funds Programme (university-level project) (Grant Nos. YC2024-032, 12362026, 62563028).

Conflicts of Interest

The authors declare no conflicts of interest regarding the publication of this paper.

References

[1] Lighthill, S.J. (1975) Mathematical Biofluiddynamics. Society for Industrial and Applied Mathematics. https://doi.org/10.1137/1.9781611970517

[2] Weihs, D. (1973) Hydromechanics of Fish Schooling. *Nature*, **241**, 290-291. https://doi.org/10.1038/241290a0

[3] Liao, J.C., Beal, D.N., Lauder, G.V. and Triantafyllou, M.S. (2003) Fish Exploiting Vortices Decrease Muscle Activity. *Science*, **302**, 1566-1569. https://doi.org/10.1126/science.1088295

[4] Beal, D.N., Hover, F.S., Triantafyllou, M.S., Liao, J.C. and Lauder, G.V. (2006) Passive Propulsion in Vortex Wakes. *Journal of Fluid Mechanics*, **549**, 385-402. https://doi.org/10.1017/s0022112005007925

[5] Wang, S., Jia, L. and Yin, X. (2008) Kinematics and Forces of a Flexible Body in Kármán Vortices. *Chinese Science Bulletin*, **53**, 2687-2691.

[6] Breder, C.M. (1954) Equations Descriptive of Fish Schools and Other Animal Aggregations. *Ecology*, **35**, 361-370. https://doi.org/10.2307/1930099

[7] Weihs, D. (1975) Some Hydrodynamical Aspects of Fish Schooling. In: Wu, T.YT., Brokaw, C.J. and Brennen, C., Eds., *Swimming and Flying in Nature*, Springer, 703-718. https://doi.org/10.1007/978-1-4757-1326-8_16

[8] Lopez, U., Gautrais, J., Couzin, I.D. and Theraulaz, G. (2012) From Behavioural Analyses to Models of Collective Motion in Fish Schools. *Interface Focus*, **2**, 693-707. https://doi.org/10.1098/rsfs.2012.0033

[9] Dai, L. (2018) Mechanism and Performance Study of Fish-Inspired Self-Propelled Motion Driven by Fluid-Structure Interaction. Institute of Mechanics, Chinese Academy of Sciences.

[10] Partridge, B.L. and Pitcher, T.J. (1979) Evidence against a Hydrodynamic Function for Fish Schools. *Nature*, **279**, 418-419. https://doi.org/10.1038/279418a0

[11] Ashraf, I., Godoy-Diana, R., Halloy, J., Collignon, B. and Thiria, B. (2016) Synchronization and Collective Swimming Patterns in Fish (*Hemigrammus bleheri*). *Journal of The Royal Society Interface*, **13**, Article 20160734. https://doi.org/10.1098/rsif.2016.0734

[12] Ashraf, I., Bradshaw, H., Ha, T., Halloy, J., Godoy-Diana, R. and Thiria, B. (2017) Simple Phalanx Pattern Leads to Energy Saving in Cohesive Fish Schooling. *Proceedings of the National Academy of Sciences*, **114**, 9599-9604. https://doi.org/10.1073/pnas.1706503114

[13] Becker, A.D., Masoud, H., Newbolt, J.W., Shelley, M. and Ristroph, L. (2015) Hydrodynamic Schooling of Flapping Swimmers. *Nature Communications*, **6**, Article No. 8514. https://doi.org/10.1038/ncomms9514

[14] Ramananarivo, S., Fang, F., Oza, A., Zhang, J. and Ristroph, L. (2016) Flow Interactions Lead to Orderly Formations of Flapping Wings in Forward Flight. *Physical Review Fluids*, **1**, Article 071201. https://doi.org/10.1103/physrevfluids.1.071201

[15] Zhu, L. and Peskin, C.S. (2002) Simulation of a Flapping Flexible Filament in a Flowing Soap Film by the Immersed Boundary Method. *Journal of Computational Physics*, **179**, 452-468. https://doi.org/10.1006/jcph.2002.7066

[16] Zhang, J., Childress, S., Libchaber, A. and Shelley, M. (2000) Flexible Filaments in a Flowing Soap Film as a Model for One-Dimensional Flags in a Two-Dimensional Wind. *Nature*, **408**, 835-839. https://doi.org/10.1038/35048530

[17] Shelley, M., Vandenberghe, N. and Zhang, J. (2005) Heavy Flags Undergo Spontaneous Oscillations in Flowing Water. *Physical Review Letters*, **94**, Article 094302. https://doi.org/10.1103/physrevlett.94.094302

[18] Shelley, M.J. and Zhang, J. (2011) Flapping and Bending Bodies Interacting with Fluid Flows. *Annual Review of Fluid Mechanics*, **43**, 449-465. https://doi.org/10.1146/annurev-fluid-121108-145456

[19] Tian, F. (2013) Role of Mass on the Stability of Flag/Flags in Uniform Flow. *Applied Physics Letters*, **103**, Article 034101. https://doi.org/10.1063/1.4813006

[20] Quinn, D.B., Lauder, G.V. and Smits, A.J. (2014) Flexible Propulsors in Ground Effect. *Bioinspiration & Biomimetics*, **9**, Article 036008. https://doi.org/10.1088/1748-3182/9/3/036008

[21] Blevins, E. and Lauder, G.V. (2013) Swimming Near the Substrate: A Simple Robotic Model of Stingray Locomotion. *Bioinspiration & Biomimetics*, **8**, Article 016005. https://doi.org/10.1088/1748-3182/8/1/016005

[22] Fernández-Prats, R., Raspa, V., Thiria, B., Huera-Huarte, F. and Godoy-Diana, R.

(2015) Large-Amplitude Undulatory Swimming Near a Wall. *Bioinspiration & Biomimetics*, **10**, Article 016003. https://doi.org/10.1088/1748-3190/10/1/016003

[23] Sun, W., He, G., Jin, F., Wang, Q. and Yu, F. (2024) Numerical Study and Parameter Prediction of a Full-Free Flexible Flament in Wakes of Flapping Wing. *Acta Mechanica Sinica*, **40**, Article 323247. https://doi.org/10.1007/s10409-023-23247-x

[24] Peskin, C.S. (1972) Flow Patterns around Heart Valves: A Numerical Method. *Journal of Computational Physics*, **10**, 252-271. https://doi.org/10.1016/0021-9991(72)90065-4

[25] Deng, J., Shao, X. and Yu, Z. (2007) Hydrodynamic Studies on Two Traveling Wavy Foils in Tandem Arrangement. *Physics of Fluids*, **19**, Article 113104. https://doi.org/10.1063/1.2814259

[26] Su, S., Lai, M. and Lin, C. (2007) An Immersed Boundary Technique for Simulating Complex Flows with Rigid Boundary. *Computers & Fluids*, **36**, 313-324. https://doi.org/10.1016/j.compfluid.2005.09.004